



OPEN

# Visible and Infra-red Light Emission in Boron-Doped Wurtzite Silicon Nanowires

SUBJECT AREAS:

NANOPHOTONICS AND  
PLASMONICS

FLUORESCENCE SPECTROMETRY

NANOWIRES

STRUCTURAL PROPERTIES

Filippo Fabbri<sup>1\*</sup>, Enzo Rotunno<sup>1</sup>, Laura Lazzarini<sup>1</sup>, Naoki Fukata<sup>2</sup> & Giancarlo Salviati<sup>1</sup><sup>1</sup>IMEM-CNR Institute, Parco area delle Scienze 37/A, Parma, (Italy), <sup>2</sup>International Center for Materials Nanoarchitectonics, National Institute for Materials Science, Tsukuba, Ibaraki, (Japan).

Received

12 June 2013

Accepted

27 November 2013

Published

8 January 2014

Correspondence and requests for materials should be addressed to F.F. (filippo.fabbri@imem.cnr.it)

\* Current address: Department of Materials Science and Engineering, Massachusetts Institute of Technology, Cambridge, MA, USA.

**Silicon, the mainstay semiconductor in microelectronic circuitry, is considered unsuitable for optoelectronic applications owing to its indirect electronic band gap, which limits its efficiency as a light emitter. Here we show the light emission properties of boron-doped wurtzite silicon nanowires measured by cathodoluminescence spectroscopy at room temperature. A visible emission, peaked above 1.5 eV, and a near infra-red emission at 0.8 eV correlate respectively to the direct transition at the  $\Gamma$  point and to the indirect band-gap of wurtzite silicon. We find additional intense emissions due to boron intra-gap states in the short wavelength infra-red range. We present the evolution of the light emission properties as function of the boron doping concentration and the growth temperature.**

Cubic bulk silicon has an indirect band gap of 1.1 eV and does not emit high intensity radiation in the visible range or at any wavelength. Light emission is found when selected active impurities (such as erbium<sup>1-3</sup>) and/or line defects (as dislocation<sup>4</sup>) and/or new phases (such as iron disilicide<sup>5</sup>) are inserted into the lattice. Room-temperature light emission from silicon has been recently reported also in low-dimensional system<sup>6-11</sup> such as nanocrystals<sup>8,11</sup>, nano-pillars<sup>12</sup>, porous silicon<sup>6,7,10</sup>, and silicon/insulator superlattices<sup>3,9</sup>.

Wurtzite (WZ) silicon has been found to be stable mainly at the nanoscale<sup>13</sup>, but the light emission properties of this material have not yet been studied in detail. Some theoretical studies<sup>14-16</sup> predict that the WZ-Si indirect band-gap is in the near infra-red range, as is the emission of the erbium related states in bulk silicon<sup>1-3</sup>, while a direct transition at  $\Gamma$  point is expected at around 1.4–1.5 eV. Should these predictions be proven and supported by experimental optical emission studies, a new scenario in the field of silicon-based rare-earth free optoelectronic devices will open. This development will have important implications not only for the scientific community, but also for the optoelectronic device market<sup>17,18</sup>.

In this letter we report on the optical properties of the wurtzite silicon nanowires (NWs), which we studied by means of room temperature cathodoluminescence spectroscopy (CL) in the visible, near infra-red and short wavelength infrared ranges (NIR, SWIR). The CL experiments reveal that wurtzite silicon NWs have about two orders of magnitude relative higher efficiency than cubic bulk silicon (Figure 1). Additional details are reported in the Supplementary Information.

Two deposition parameters, the boron precursors flow and the growth temperature (summarized in Supplementary Information Figure S1), are varied in order to clarify their influence on the optical, structural and morphological properties of the NWs. We will identify each sample with the letter B and the corresponding value of the diborane flow (for example B1.0), while the sample grown at lower temperature will be named T550°.

## Results

High resolution transmission electron microscopy (HRTEM) imaging and electron diffraction correlate the effect of the boron doping with the NW crystalline structure as well as the presence of crystal defects, fundamental for the CL emissions attribution.

In addition to hexagonal NWs, depending on the diborane flow, different concentrations of cubic NWs are observed. Figure 2a shows the statistics of the TEM observations of the crystal structure of the NWs under analysis; these statistics are based on the observation of more than 40 different NWs for each sample, so the statistical error is  $\pm 15\%$ . The statistics of the sample T550° (not shown) are consistent with that of the sample B0.2.

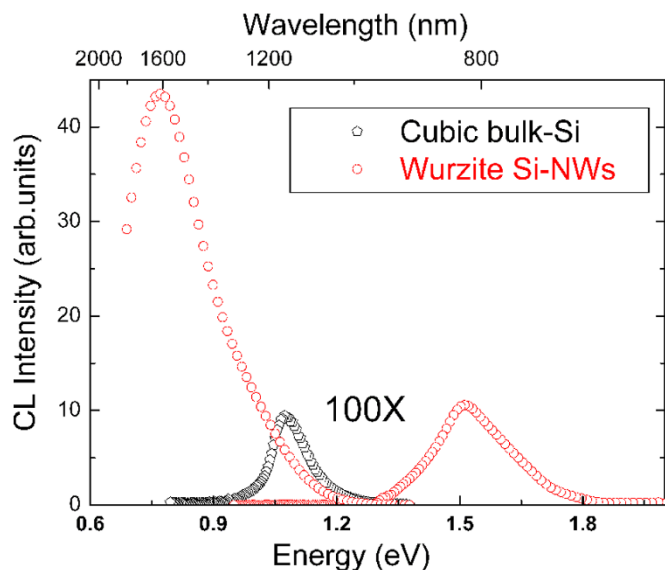


**Figure 1** | Comparison between CL spectra of wurtzite SiNWs and standard cubic silicon. It is worth noting that it is not possible compare the integrated intensities of the visible and NIR emissions because they are obtained with different amplification parameters.

As a general comment, the TEM statistics shows that decreasing the diborane flow results in an increase of the hexagonal phase and a concurrent decrease of the cubic one. In addition, increasing the diborane flow induces an increase of the cubic phase as well as of the percent of defective (flawed) nanowires.

Figure 2b shows the low magnification TEM image of a 30 nm thick Si nanowire, grown along the (1–100) direction of the hexagonal lattice, taken from the sample B0.5. All the hexagonal wires grow along this direction in agreement with previous works<sup>19</sup>. The dark particle on the top is the Au metal catalyst. A HRTEM image of the red marked region is shown in Fig. 2c, left panel. The reported lattice distance of 0.33 nm corresponds to the (1–100) interplanar distance of the hexagonal Silicon phase. Fig. 2c (right panel) shows the image simulation for a 30 nm thick wurtzite Si sample, in the [0001] projection. A perfect match is found between the simulation and the experiment. The microscope parameters used to mimic the experimental condition are reported in the figure caption.

According to some authors, a wrong attribution to the wurtzite phase is possible if the TEM images are misinterpreted in presence of defects in the cubic phase that can produce the same fringes and diffraction patterns as in the hexagonal structure. As a matter of fact, a twin plane orthogonal to the (111) direction in cubic silicon originates misleading fringes when observed along this direction that do not change even if the sample is rotated widely apart<sup>20</sup> while a tangled set of micro- and nanotwin, hidden inside the body of the NW, is responsible for the extra spots commonly observed in the diffraction patterns<sup>20,21</sup>.

In order to avoid misinterpretation, we took great care to choose the appropriate geometry in our HRTEM and diffraction patterns studies to assess the correct crystal phase, comparing these studies to appropriate simulations<sup>22</sup>. See Supplementary information Fig. S2–5. As a result, we are able to distinguish between a HREM pattern coming from a bi-twin cubic crystal and a hexagonal one, but not between different hexagonal polytypes. As a matter of fact, as shown by Arbiol<sup>23,24</sup> and Lopez<sup>19</sup>, different hexagonal polytypes, originating from the periodic ordering of stacking faults along the [111]

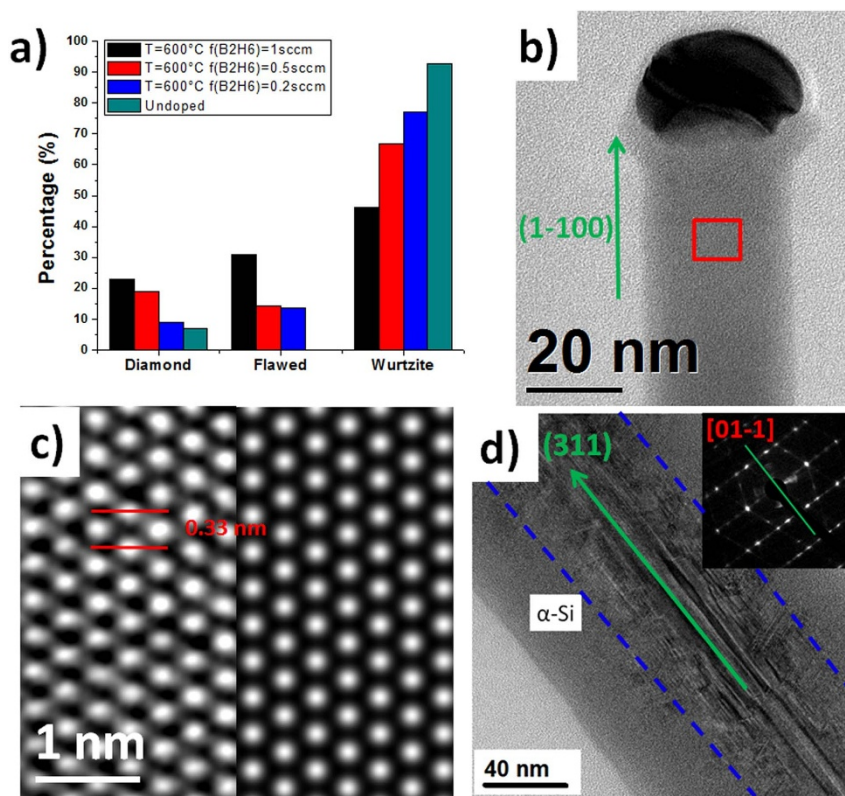


**Figure 2** | HRTEM analysis of silicon nanowires. a) statistical distribution of the different typologies of wires found in the samples investigated. b) [0001] zone axis low magnification TEM experimental image of a WZ Si NW, growing along the (1–100) direction (green arrow). c) left enlargement of the red squared area in a), right image simulation of the IVa silicon Wurtzite structure in the same projection ( $E_b = 200$  keV, defocus = 45 nm,  $C_s = 0.5$  mm); d) [011] type projection of a “flawed” cubic silicon NW showing a twin parallel to the [–2–11] direction (green arrow), corresponding to the growth direction (green arrow). The inset shows the FFT.



irection, can coexist in the same wire. These structures also can be responsible of the experimental TEM observation we report on in this work<sup>25</sup>.

The identification of the polytypes can be performed by imaging in the (11–20) projection. However, during the TEM observations on hundreds of NWs of different length and diameter, we did not find it, due to the lateral growth induced by the boron doping that causes our NWs to have an ellipsoidal section rather than circular. For this reason, our NWs lie preferentially on the (0001) plane when deposited on the TEM grids: this plane is orthogonal to the (11–20) one, therefore unattainable by the tilting range of our microscope.

The TEM analyses also reveal the existence of a second type of NWs we call “flawed NWs” to distinguish them from the perfect wurtzite and cubic ones, taken from sample B1.0. They appear to be seriously defective (Fig. 2d) but a careful inspection shows that they have a cubic Si core, grown along the (–211) direction, embedded in a thick, amorphous Si shell. At the interface, highlighted with blue dashed line, the cubic core fades into the amorphous shell through many arrays of short stacking faults along the (111) directions. In the middle of the wires at least one twin plane is always present all along the NW length, parallel to the growth direction.

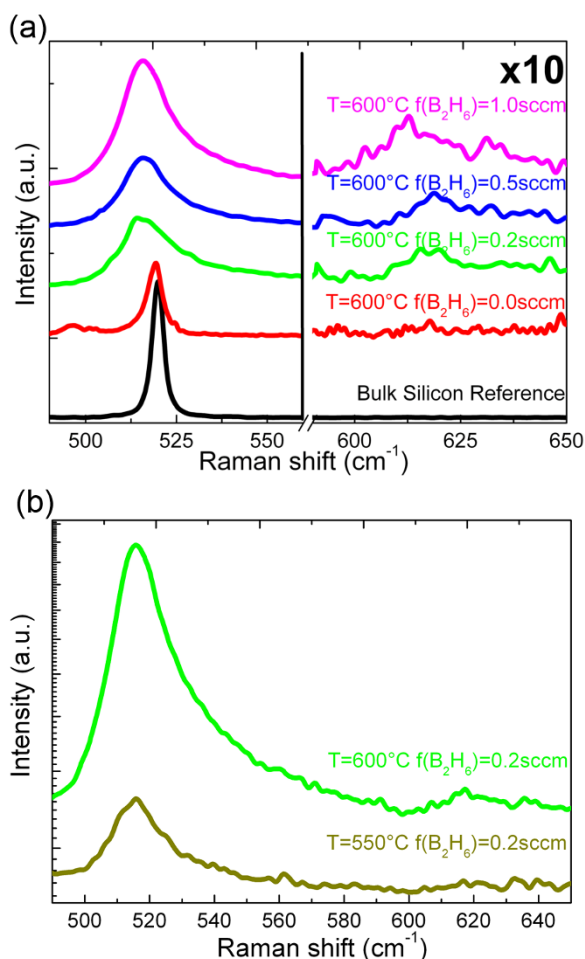


**Figure 3** |  $\mu$  Raman analyses of the undoped and boron doped NWs in comparison with a cubic bulk silicon spectrum (black line). These spectra report about the doping related broadening of the optical phonon peak due to the Fano resonance effect. In addition a clear shoulder on the low wavenumber side appears in all the spectra of the NWs. The additional peak is set at  $495\text{ cm}^{-1}$ , as clearly visible in particular in the spectrum of the undoped NWs. Figure 2b reports the  $\mu$  Raman analysis of the NWs grown at different temperature with the same diborane flow. The plot is reported in semi-log scale.

Micro-Raman spectroscopy is used mainly to evaluate the boron doping by Fano broadening fitting procedures. It must be stressed that, to the best of our knowledge, no theoretical and/or experimental results have ever been reported on this aspect in the case of wurtzite silicon. The approach we used, therefore, was to compare our data with the data collected for cubic bulk silicon doped with high boron concentration. We are aware that this approach could result in over-estimation of the doping concentration. In addition, the attribution of the optical phonons peak wavenumber is not straightforward because the wavenumber positions of the optical phonons peaks of wurtzite silicon are still an open issue<sup>13,26–29</sup>.

Figure 3a shows the Raman spectra of the B-series. The Raman spectrum of the undoped NWs shows two peaks set at  $519\text{ cm}^{-1}$ , and at  $495\text{ cm}^{-1}$ , while the spectra related to the boron-doped NWs show only one broad peak set at about  $515\text{ cm}^{-1}$ . The positions of these peaks are consistent with those reported from Raman studies on wurtzite silicon nanostructures<sup>27,28</sup>. The overlap of the two optical phonon peaks, in the case of B-doped NWs, is ascribed to the peak broadening due to Fano resonance effect<sup>30,31</sup>. However  $515\text{ cm}^{-1}$  is even the TO position reported in the case of highly doped cubic silicon as shown in<sup>32,33</sup>.

Based on the Raman data, we estimate the doping concentration by comparing the fitting parameters of the Fano equation (reported in Supplementary Information) to those reported for highly boron doped cubic bulk silicon<sup>32,33</sup>.

The doping concentration is evaluated to vary between  $0.7$  to  $1.6 \times 10^{20}\text{ cm}^{-3}$ , for the B series. As already mentioned, the doping concentration could be overestimated due to a possible phonon confinement effect resulting from the size of the NWs tips<sup>34,35</sup>, that would affect the TO peak position, and to the aforementioned convolution effect, that would affect the asymmetry factor  $q$ .

The micro-Raman analyses reveal that the growth temperature has a significant effect on the relative intensity of the silicon optical phonon peak, that is, the crystalline quality of the NWs (reported in Figure 3b).

The  $q$  and  $\Gamma$  values (last line of Table 1) indicate that the doping concentration for T550°C is  $6 \times 10^{19}\text{ cm}^{-3}$ <sup>33</sup>, lower than that for sample B0.2.

In addition, micro-Raman spectra present two peaks set at  $620\text{ cm}^{-1}$  and  $638\text{ cm}^{-1}$  which are related to substitutional boron isotopes ( $^{11}\text{B}$  and  $^{10}\text{B}$ ) respectively<sup>31</sup>. The relative intensities of these two peaks are comparable in all the samples suggesting, a similar doping concentration. By comparing the  $620\text{ cm}^{-1}$  and  $638\text{ cm}^{-1}$  peaks intensities in the micro-Raman analysis, we notice that there is no clear effect on the concentration of substitutional boron atoms. On the contrary, the increase of the  $q$  value suggests a lower electrical activation of the boron atoms. This effect is consistent with the morphological data from which we see, that the increase of the diborane flow results in an increase of the wire tapering effect (Supplementary Information Figure S7 and S8), which is caused by a boron-induced lateral growth as demonstrated in the case of Ge NWs by Fukata et al.<sup>36</sup>. In addition the reported amorphization (Supplementary Information Figure S8) of the NWs is probably induced by the deposition of boron atoms on the surface<sup>37</sup>. The lower electrical active doping concentration of the NWs is also supported by the lower relative intensities of the boron-related peaks at

**Table 1** | summarizes the values of the asymmetry parameter  $q$  and of the line width parameter  $\Gamma$

Sample	$q$ ( $\text{cm}^{-1}$ )	$\Gamma$ ( $\text{cm}^{-1}$ )
B0.2	4.8	8.5
B0.5	7.4	8.7
B1.0	7.3	8.4
T550°	10	6.2



618  $\text{cm}^{-1}$  and 640  $\text{cm}^{-1}$ . As expected, the Raman analyses confirm that the temperature is an important parameter in the activation of the boron dopants in silicon NWs.

A room temperature CL spectrum is reported with the deconvolution Gaussian peaks in Figure 4a and Figure 4b for the visible, NIR range and for the SWIR respectively. All the integrated intensities for the reported spectra are summarized in Table S2 of the Supplementary Information. We cannot compare the integrated intensities of the visible and NIR emissions because they are obtained with different amplification parameters (See experimental details reported in the Supplementary Information). In the visible range, all the spectra of the B series show a band peaked at 1.55 eV with a shoulder on the high-energy side, reported in Figure 5a. The integrated intensity of this band remains almost constant in all the samples. The emission energy of the shoulder is found to be 1.68 eV. This emission can be ascribed to amorphous silicon<sup>38</sup> and/or to under-stoichiometric silicon dioxide<sup>39</sup>. Considering the TEM results, the trend of the integrated intensity of the peak at 1.68 eV and the

increase of the flawed NWs density that we find, we are inclined to ascribe this transition to amorphous silicon. The CL panchromatic map of the NWs is reported in Figure S9 of the Supplementary Information.

In the following, we will discuss the NIR emission range of our CL spectra. A careful inspection reveals that the NWs emission is strongly dependent on the  $\text{B}_2\text{H}_6$  flow. Except for the undoped NW, the NIR integrated intensities are in inverse proportion to the diborane flow. It is worth noting that the change of slope suggests the presence of a shoulder on the high-energy side. Accurate deconvolution procedures show that the additional peak is centered at about 0.92 eV (See Figure 4a and 4b).

Because the luminescence increases toward the low-energy side and the Ge detector energy range is limited, we have to use an InGaAs extended-range detector in order to study the complete lineshape of the spectrum (Figure 5b).

As for the SWIR range, the CL analyses show that the main emission peak is set at about 0.6 eV. Also for this energy range the dependence of the NWs emission on the diborane flow is consistent with the NIR range previously presented. The difference in intensity for the 0.92 eV peak is mainly due to the different detectors' sensitivity. In addition the main peak in the short wavelength infrared range analyses seem to be composed of two different features, i.e., the main peak at 0.6 eV and an additional peak at about 0.75 eV.

In the following we provide an attribution to each peak by making an accurate comparison with previous theoretical and experimental work.

## Discussion

Different theoretical studies calculate the band-gap of wurtzite silicon, with the work of Joannopoulos and Cohen, the first one reported<sup>15</sup>. Using empirical pseudopotential method, these authors found that the wurtzite silicon has an indirect bandgap set at about 0.8 eV, narrower than that of cubic silicon. The direct transition at the  $\Gamma$  point is predicted to be at 1.4 eV and at 4.2 eV for wurtzite and cubic silicon, respectively<sup>15,40</sup>. The band diagram for wurtzite silicon is reported in Figure S10 of the Supplementary Information. Recently other groups have faced the problem of evaluating the wurtzite silicon bandgap. Persson and Janzen performed calculations based on the density functional theory, applying the local density approximation<sup>16</sup>, and obtained an indirect band-gap at 0.99 eV and 1.17 eV for wurtzite and cubic silicon, respectively. Raffy et al. reported similar calculations, finding 0.29 eV and 0.54 eV, (without any rigid correction to the band-gap calculation) values in the case of wurtzite and cubic silicon<sup>14</sup>. These values give rise to a value of the indirect band-gap of about 0.92 eV and 1.17 eV for wurtzite and cubic silicon, respectively. Comparing the aforementioned theoretical predictions with our results, we find that the evaluation of the direct transition of the  $\Gamma$  point agrees with the 1.55 eV emission. Experimentally Bandet et al. report a photoluminescence emission for wurtzite Si/SiO<sub>2</sub> core/shell nanoparticles covered set at 1.45 eV with a lineshape similar to the one that we find but slightly red-shifted to lower energy<sup>28</sup>.

In the case of the indirect bandgap the attribution to the 0.92 eV emission is consistent with previous findings<sup>14,16</sup>. All the theoretical and experimental results are summarized in Table S2, in the Supplementary Information.

Considering the NIR and short wavelength IR emissions, no experimental data and/or theoretical predictions are reported in the literature for intra-gap states of wurtzite silicon. Therefore, it is difficult to attribute the emission peaks to intrinsic or extrinsic intra-gap states. However, we propose that the 0.6 eV emission could be related to boron induced level in wurtzite silicon because of the dependence of the CL emission integrated intensity on the diborane flow. The Raman analyses show a similar intensity of boron substitutional atoms related peaks, therefore we cannot assign the 0.6 eV

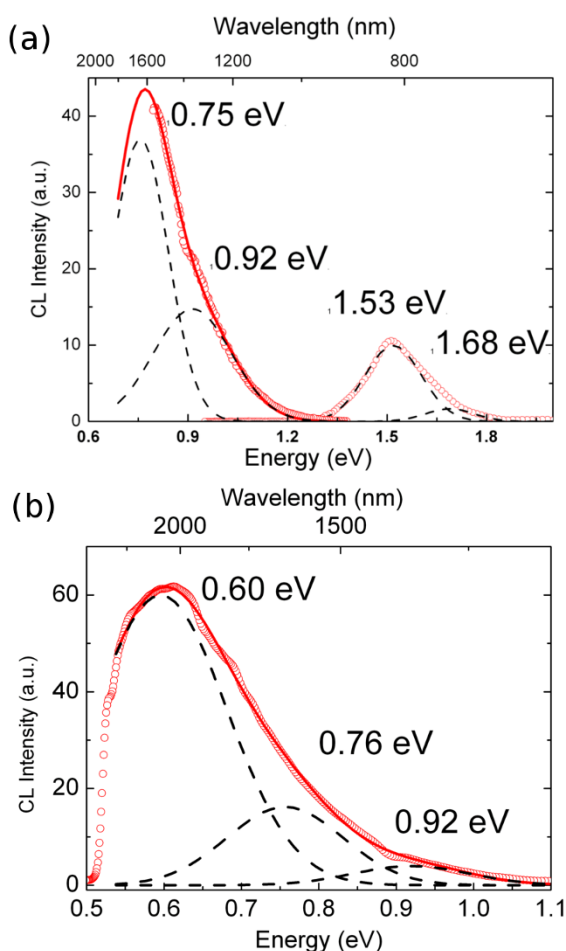


**Figure 4** | CL spectrum in different wavelength ranges, deconvoluted with Gaussian peaks. In the case of the visible-NIR spectrum the Gaussian deconvolution procedure reveals two features at 1.68 eV and at 1.53 eV in the visible range and two in the NIR range peaked at 0.92 eV and at 0.75 eV. Due to the cut of the Ge detector, the authors used the InGaAs extended range detector in order to understand the line shape of the spectrum beyond the 0.7 eV, and in order to enlarge the study to the short wavelength infra-red range. Another feature peaked at about 0.6 eV appears as reported in Figure S11b. The fitting procedure and the spectral resolution of our system give an uncertainty of the energy value that is of the 10%. It is worth noting that it is not possible to compare the integrated intensities of the visible and NIR emissions because they are obtained with different amplification parameters.

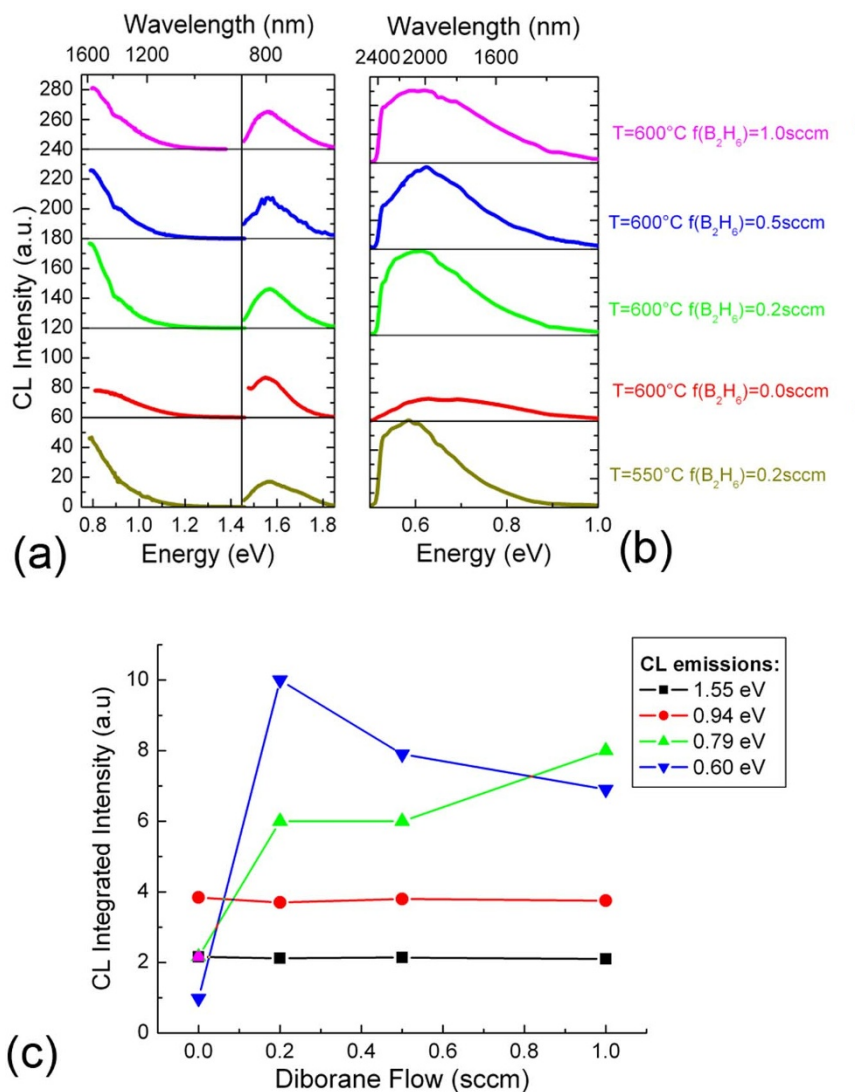


**Figure 5** | CL spectrum in different wavelength ranges for the sample in analysis (a) CL spectra of the NWs grown with an increasing diborane flow, from 0.0 to 1.0 sccm and at different temperature, in the visible/NIR range. (b) CL spectra of the same NWs in the NIR/short wavelength IR. (c) dependence of the integrated intensities of the different emissions as a function of the diborane flow. The dependence of the 0.75 eV and 0.6 eV bands to the diborane flow suggests that these emissions are related to boron intra-gap states.

peak to the boron shallow acceptor state. In fact it is more likely that the boron shallow state is related to the emission peaked at 0.75 eV. The ionization energy, obtained as the difference between the optical band-gap and the peak energy, is 170 meV. This value is larger than the case of boron doping in cubic silicon (45 meV)<sup>41</sup>. Because of the high boron concentration obtained from the Fano broadening procedure, (next to the solid solubility limit for boron in silicon<sup>42</sup>), we can suggest that the boron shallow acceptor state is a broad energy band and that boron-complex related states are present.

A comparison with others findings for boron-related complexes in cubic silicon, we suggest a possible attribution of the 0.6 eV states. Mooney et al. propose two possible boron complex structures to explain the presence of a boron related state set around 0.27 eV above the valence band. These authors attribute this level to a complex made by an interstitial boron atom bonded to an interstitial oxygen atom or by a silicon vacancy bonded to substitutional boron in silicon<sup>43</sup>. Figure 3c summarizes the integrated intensities of the different peaks as a function of the diborane flow. The emission related to a direct transition at the  $\Gamma$  point and that related to the indirect band-gap have similar integrated intensities for the B series. On the contrary, the bands at 0.75 eV and 0.6 eV show a clear trend. When we increase the diborane flow the integrated intensity of the

band peaked at 0.75 eV increases, meanwhile the 0.6 eV peak is highest at 0.2 sccm and then decreases. The increase of the 0.75 eV suggests that the sample B1.0 has a slightly higher boron doping concentration than the other samples, even if the Raman analyses do not show this effect. The decrease of 0.6 eV emission integrated intensity can reasonably be related to a different concentration of the boron-complexes in the different samples.

The lower crystalline quality of the NWs grown at lower temperature suggested by the Raman analyses is confirmed by the CL spectroscopy studies. In fact the sample T550° presents the visible emission, previously attributed to the direct transition at the  $\Gamma$  point (Figure 3b), with a lower intensity when we compare it to the sample B0.2. We see similar effect in the NIR range: the peak at 0.92 eV, related to the indirect band-gap, has a lower intensity for the sample T550°.

The SWIR analysis agrees with that described above and, moreover, reveals that the peak at 0.75 eV has a lower intensity, as expected, due to the lower activation of the dopant found by Raman experiments. It is worth noting that the peak at 0.6 eV has a similar intensity for both samples. This means that the formation of the boron complexes, gives rise to the light emission at 0.6 eV, depending mainly on the amount of boron present during the growth process and not on the growth temperature.



In conclusion we report on the light emission properties of wurtzite silicon nanowires doped with boron. This work shows that the wurtzite silicon can be an interesting material to develop silicon based optoelectronic devices due to strong light emissions, about three orders of magnitude higher than bulk silicon.

We carry out our study in different wavelength/energy ranges in order to fully clarify the optical properties of wurtzite silicon NWs. We conduct the study using different parameters, as the boron precursor flow and the growth temperature. The structural characterization reveals that when we increase the diborane flow, the amount of perfect crystalline NWs decreases drastically, and concurrently the amount of defective/amorphous NWs increases. We investigate the dopant concentration and show that the increase of the diborane flow induces a decrease of the dopant concentration due to boron atom clustering effects. These results are reflected in the CL characterization that demonstrates, in principle, that wurtzite silicon NWs have interesting light emission properties, because they show an intense emission in the visible range (at about 1.5 eV) related to the direct transition at the  $\Gamma$  point. Moreover, we find an emission in the near infra-red range at about 0.92 eV, probably related to the indirect band-gap of this material. This finding is supported by theoretical calculations from the literature. Different emissions in the short wavelength infra-red range due to intra-gap states are also reported. The peaks at 0.75 eV and at 0.6 eV are ascribed to boron shallow acceptors and to boron complexes respectively.

## Methods

The Si NWs are synthesized by means of a metal-catalyzed vapor-liquid-solid (VLS) growth mechanism<sup>31,44</sup> in a commercial chemical vapour deposition (CVD) system directly onto (111) Si single crystal substrates. Gold nanocolloidal particles of 3 nm in diameter are used as metal catalyst. Undoped and B-doped NWs are directly grown onto Si substrates at a temperature of 550 °C or of 600 °C for 30 min in flowing 19 sccm of SiH<sub>4</sub> as the silicon reactant gas and the diborane (B<sub>2</sub>H<sub>6</sub>) is used as boron precursor. The B<sub>2</sub>H<sub>6</sub> flow is varied between 0.2 to 1.0 sccm in H<sub>2</sub> and 30 sccm of nitrogen (N<sub>2</sub>) as the carrier gas. The resuming graph of the growth parameters is shown in the Supplementary information (Figure S2).

High resolution transmission electron microscopy (HRTEM) investigations are carried out in a JEOL JEM 2200FS equipped with in column omega filter, two high angle annular dark field detectors system. The NWs have been removed by the deposited samples, dispersed in isopropanol, sonicated and then dispersed on holey carbon copper grids for TEM observations.

Micro-Raman scattering measurements are performed at room temperature with a 100× objective and a 532 nm excitation light. The excitation power was set to about 30 μW to prevent local heating.

Cathodoluminescence spectroscopy is carried out in a S360 Cambridge SEM equipped with a commercial Gatan monoCL system. The spectra are collected at an accelerating voltage of 7.5 keV with a beam current of 115 nA.

1. Franzo, G., Priolo, F., Coffa, S., Polman, A. & Carnera, A. Room-temperature electroluminescence from Er-doped crystalline Si. *Appl Phys Lett* **64**, 2235–2237 (1994).
2. Cavallini, A. *et al.* Electrical and optical characterization of Er-doped silicon grown by liquid phase epitaxy. *J Appl Phys* **85**, 1582–1586 (1999).
3. Cuffe, S. *et al.* Investigation of emitting centers in SiO<sub>2</sub> codoped with silicon nanoclusters and Er<sup>3+</sup> ions by cathodoluminescence technique. *J Appl Phys* **108**, 113504–113508 (2010).
4. Kveder, V. V., Steinman, E. A., Shevchenko, S. A. & Grimmeiss, H. G. Dislocation-related electroluminescence at room temperature in plastically deformed silicon. *Phys Rev B* **51**, 10520–10526 (1995).
5. Leong, D., Harry, M., Reeson, K. J. & Homewood, K. P. A silicon/iron-disilicide light-emitting diode operating at a wavelength of 1.5 μm. *Nature* **387**, 686–688 (1997).
6. Canham, L. T. Silicon quantum wire array fabrication by electrochemical and chemical dissolution of wafers. *Appl Phys Lett* **57**, 1046–1048 (1990).
7. Cullis, A. G. & Canham, L. T. Visible light emission due to quantum size effects in highly porous crystalline silicon. *Nature* **353**, 335–338 (1991).
8. Wilson, W. L., Szajowski, P. F. & Brus, L. E. Quantum Confinement in Size-Selected, Surface-Oxidized Silicon Nanocrystals. *Science* **262**, 1242–1244 (1993).
9. Lu, Z. H., Lockwood, D. J. & Baribeau, J. M. Quantum confinement and light emission in SiO<sub>2</sub>/Si superlattices. *Nature* **378**, 258–260 (1995).
10. Hirschman, K. D., Tsybeskov, L., Duttgupta, S. P. & Fauchet, P. M. Silicon-based visible light-emitting devices integrated into microelectronic circuits. *Nature* **384**, 338–341 (1996).

11. Pavesi, L., Dal Negro, L., Mazzoleni, C., Franzo, G. & Priolo, F. Optical gain in silicon nanocrystals. *Nature* **408**, 440–444 (2000).
12. Nassiopoulou, A. G., Grigoropoulos, S. & Papadimitriou, D. Electroluminescent device based on silicon nanopillars. *Appl Phys Lett* **69**, 2267–2269 (1996).
13. Fontcuberta i Morral, A., Arbiol, J., Prades, J. D., Cirera, A. & Morante, J. R. Synthesis of Silicon Nanowires with Wurtzite Crystalline Structure by Using Standard Chemical Vapor Deposition. *Adv Mater* **19**, 1347–1351 (2007).
14. Raffy, C., Furthmüller, J. & Bechstedt, F. Properties of hexagonal polytypes of group-IV elements from first-principles calculations. *Phys Rev B* **66**, 075201 (2002).
15. Joannopoulos, J. D. & Cohen, M. L. Electronic Properties of Complex Crystalline and Amorphous Phases of Ge and Si. I. Density of States and Band Structures. *Phys Rev B* **7**, 2644–2657 (1973).
16. Persson, C. & Janzén, E. Electronic band structure in hexagonal close-packed Si polytypes. *J Phys-Condens Mat* **10**, 10549 (1998).
17. Reuters, China, a Rare Earths Giant, Set to Start Importing the Elements (08/2012) *New York Times* <http://www.nytimes.com/2012/07/12/business/global/china-a-rare-earths-giant-set-to-start-importing-the-elements.html?ref=rareearths&r=1&>.
18. Ching, N. Rare Earths in *New York Times* (06/2012) [http://topics.nytimes.com/top/reference/timestopics/subjects/r/rare\\_earths/index.html](http://topics.nytimes.com/top/reference/timestopics/subjects/r/rare_earths/index.html).
19. Lopez, F. J., Hemesath, E. R. & Lauhon, L. J. Ordered Stacking Fault Arrays in Silicon Nanowires. *Nano Letters* **9**, 2774–2779 (2009).
20. Kohno, H., Ozaki, N., Yoshida, H., Tanaka, K. & Takeda, S. Misleading fringes in TEM images and diffraction patterns of Si nanocrystallites. *Crys Res Technol* **38**, 1082–1086, doi:10.1002/crat.200310140 (2003).
21. Cayron, C. *et al.* Odd electron diffraction patterns in silicon nanowires and silicon thin films explained by microtwins and nanotwins. *J Appl Crystallogr* **42**, 242–252 (2009).
22. Grillo, V. & Rotunno, E. STEM\_CELL: A software tool for electron microscopy: Part I—simulations. *Ultramicroscopy* **125**, 97–111 (2013).
23. Arbiol, J., Kalache, B., Cabarrocas, P. R. i., Morante, J. R. & Morral, A. F. i. Influence of Cu as a catalyst on the properties of silicon nanowires synthesized by the vapour–solid–solid mechanism. *Nanotechnology* **18**, 305606 (2007).
24. Arbiol, J. *et al.* Influence of the (111) twinning on the formation of diamond cubic/diamond hexagonal heterostructures in Cu-catalyzed Si nanowires. *J Appl Phys* **104**, 064312–064317 (2008).
25. Hemesath, E. R., Schreiber, D. K., Kisielowski, C. F., Petford-Long, A. K. & Lauhon, L. J. Atomic structural analysis of nanowire defects and polytypes enabled through cross-sectional lattice imaging. *Small* **8**, 1717–1724 (2012).
26. Prades, J. D., Arbiol, J., Cirera, A., Morante, J. R. & Fontcuberta i Morral, A. Concerning the 506 cm<sup>-1</sup> band in the Raman spectrum of silicon nanowires. *Appl Phys Lett* **91**, 123107–123103 (2007).
27. Lopez, F. J., Givan, U., Connell, J. G. & Lauhon, L. J. Silicon Nanowire Polytypes: Identification by Raman Spectroscopy, Generation Mechanism, and Misfit Strain in Homostructures. *ACS Nano* **5**, 8958–8966 (2011).
28. Bandet, J., Despax, B. & Caumont, M. Vibrational and electronic properties of stabilized wurtzite-like silicon. *J Phys D Appl Phys* **35**, 234 (2002).
29. Hertog, M. I. d. *et al.* Hidden defects in silicon nanowires. *Nanotechnology* **23**, 025701 (2012).
30. Fano, U. Effects of Configuration Interaction on Intensities and Phase Shifts. *Phys Rev* **124**, 1866–1878 (1961).
31. Fukata, N. *et al.* Segregation Behaviors and Radial Distribution of Dopant Atoms in Silicon Nanowires. *Nano Letters* **11**, 651–656, doi:10.1021/nl103773e (2011).
32. Cerdeira, F., Fjeldly, T. A. & Cardona, M. Effect of Free Carriers on Zone-Center Vibrational Modes in Heavily Doped p-type Si. II. Optical Modes. *Phys Rev B* **8**, 4734–4745 (1973).
33. Chandrasekhar, M., Chandrasekhar, H. R., Grimsditch, M. & Cardona, M. Study of the localized vibrations of boron in heavily doped Si. *Phys Rev B* **22**, 4825–4833 (1980).
34. Fukata, N. *et al.* Doping and hydrogen passivation of boron in silicon nanowires synthesized by laser ablation. *Appl Phys Lett* **89**, 203109–203103 (2006).
35. Piscanec, S. *et al.* Raman spectroscopy of silicon nanowires. *Phys Rev B* **68**, 241312 (2003).
36. Fukata, N. *et al.* Doping and Raman Characterization of Boron and Phosphorus Atoms in Germanium Nanowires. *ACS Nano* **4**, 3807–3816 (2010).
37. Pan, L., Lew, K.-K., Redwing, J. M. & Dickey, E. C. Effect of diborane on the microstructure of boron-doped silicon nanowires. *J Cryst Growth* **277**, 428–436 (2005).
38. Qin, G. G. *et al.* Experimental evidence for luminescence from silicon oxide layers in oxidized porous silicon. *Phys Rev B* **54**, 2548–2555 (1996).
39. Tong, S., Liu, X.-n. & Bao, X.-m. Study of photoluminescence in nanocrystalline silicon/amorphous silicon multilayers. *Appl Phys Lett* **66**, 469–471 (1995).
40. Siklitsky, V. Electronic archive: New Semiconductor Materials. Characteristics and Properties (01/1998–2001) <http://www.ioffe.rssi.ru/SVA/NSM/Semicond/Si/bandstr.html>.
41. Chen, J. W. & Milnes, A. G. Energy Levels in Silicon. *Annu Rev Mater Sci* **10**, 157–228 (1980).
42. Masetti, G., Severi, M. & Solmi, S. Modeling of carrier mobility against carrier concentration in arsenic-, phosphorus-, and boron-doped silicon. *IEEE T Electron Dev* **30**, 764–769 (1983).



43. Mooney, P. M., Cheng, L. J., Süli, M., Gerson, J. D. & Corbett, J. W. Defect energy levels in boron-doped silicon irradiated with 1-MeV electrons. *Phys Rev B* **15**, 3836–3843 (1977).
44. Fukata, N. *et al.* Characterization of Impurity Doping and Stress in Si/Ge and Ge/Si Core-Shell Nanowires. *ACS Nano* **6**, 8887–8895 (2012).

## Acknowledgments

This work has been partly supported by the Significant Project of the Italian Ministry of Foreign Affairs “Nanoscale evaluation of the chemical, magnetic and structural properties of advanced nanostructures (NEMESIS)”. The authors are grateful to Prof. Takashi Sekiguchi for the fruitful discussion. Dr. Fabbri wants to acknowledge Prof. Silvija Gradecak for the fruitful discussion about the NWs morphology. All the authors want to thank Attolight (Lausanne Switzerland) for the collaboration in the CL imaging of the silicon nanowires.

## Author contributions

F.F. and E.R. wrote the main manuscript text and F.F. prepared the figures 1, 3–5 E.R. prepared figure 2. The Raman and CL experiments have been carried out by F.F. The HRTEM and related simulations are carried out by E.R. L.L. supervised the HRTEM analysis, G.S. supervised the CL analysis and N.F. supervised the nanowires growth and the Raman characterization. All authors reviewed the manuscript.

## Additional information

**Supplementary information** accompanies this paper at <http://www.nature.com/scientificreports>

**Competing financial interests:** The authors declare no competing financial interests.

**How to cite this article:** Fabbri, F., Rotunno, E., Lazzarini, L., Fukata, N. & Salviati, G. Visible and Infra-red Light Emission in Boron-Doped Wurtzite Silicon Nanowires. *Sci. Rep.* **4**, 3603; DOI:10.1038/srep03603 (2014).



This work is licensed under a Creative Commons Attribution-NonCommercial-NoDerivs 3.0 Unported license. To view a copy of this license, visit <http://creativecommons.org/licenses/by-nc-nd/3.0>